

Predicting the sliding bubble velocity on the lower part of a horizontal tube heater under natural convection based on force balance analysis

Jae Soon Kim^a, Yu-Na Kim^b, Hyoung Kyu Cho^{a,*}

^a Department of Nuclear Engineering, Seoul National University, Daehak-dong, Gwanak-gu, Seoul 151-742, Republic of Korea

^b Korea Atomic Energy Research Institute, 989-111 Daedeok-daero, Yuseong-gu, Daejeon 305-353, Republic of Korea



ARTICLE INFO

Article history:

Received 11 October 2019

Revised 6 January 2020

Accepted 29 January 2020

Available online 5 March 2020

Keywords:

Boiling heat transfer

Heat partitioning model

Horizontal tube

Sliding bubble

Force balance

Bubble velocity

ABSTRACT

The main objectives of this work are to examine the sliding bubble behaviour outside a horizontal tube through a visualisation experiment and to establish a force balance model for predicting the sliding bubble velocity. Of interest here, the sliding bubble velocity is included in a mechanistic boiling heat transfer model and it varies with the bubble volume, location of the nucleation site, generation frequency of the bubble, etc. In order to predict the sliding velocity of the bubbles generated under the various conditions, a model developed based on the physical mechanism is required. This paper presents experimental techniques and measurement results for observing vapour bubble sliding phenomena. A specially devised flexible heater was fabricated and attached on a rod in order to control the bubble generation location. With the heater and a digital image processing technique, accurate measurement of the bubble volume and velocity became facilitated. Through the experiment, the life cycles of a single bubble was clearly visualised including the birth, departure, sliding, and lift-off. The force balance model which includes the curvature effect in cylindrical coordinate was derived to predict the sliding bubble velocity in the experiment. The equation of the model was based on the balance of circumferential directional forces acting on a sliding bubble with a correction of the local liquid velocity to consider the wake generated by a preceding bubble. The force balance analysis showed that the dominant forces are the buoyancy, quasi-steady drag, and added mass forces. The proposed model was validated by comparing the predicted bubble velocity with the experimental data and it predicted the bubble velocity with satisfactory accuracy. In addition, the force balance analysis found that the sliding bubble velocity correlates well with the bubble generation location when it was non-dimensionalised in a form of Froude number.

© 2020 Elsevier Ltd. All rights reserved.

1. Introduction

Precisely predicting the boiling heat transfer is important for analysing the safety of a nuclear reactor because it takes place in various components (e.g., the reactor core, steam generator, and heat exchangers of safety systems) of the system under both normal and transient conditions. Recently, new passive safety concepts have been proposed to enhance the system's performance and reliability [1] that mostly incorporate shell-and-tube type heat exchangers in various configurations. In order to evaluate their performance accurately and confirm the integrity of a nuclear reactor at the time of an accident, the heat transfer phenomena in these heat exchangers need to be investigated. Especially, the boiling phenomena within the heat exchanger geometry need to be

examined experimentally and analytically because the heat transfer is significantly dependent on the configuration.

The present study focused on the boiling heat transfer on the outer surface of a horizontal tube. This occurs frequently in industrial-purpose shell-and-tube type heat exchangers for which the shell side is a heat sink where boiling occurs. Particularly in the nuclear industry, this phenomenon is utilised to remove the decay heat that is generated in the reactor core in transient and accident situations. For example, APR+ (an advanced GEN-III reactor developed by Korea Hydro and Nuclear Power (KHNP)) is equipped with a passive auxiliary feedwater system (PAFS) [1]. PAFS incorporates a heat exchanger comprising horizontal U-tube bundles submerged in a large water pool and is connected to the secondary side of the steam generator, as shown in Fig. 1. During an accident, the steam generated in the steam generator transfers to the heat exchanger. It flows inside the heat exchanger tubes, condenses, and then returns to the steam generator by the gravity. Meanwhile, the heat of the condensation is released to the water pool through the

* Corresponding author.

E-mail addresses: godot@snu.ac.kr (J.S. Kim), ynkim@kaeri.re.kr (Y.-N. Kim), chohk@snu.ac.kr (H.K. Cho).

Nomenclature

A	cross-section of a bubble
A	linear acceleration
C_D	coefficient of drag
C_p	specific heat
d_w	contact diameter
F	force
f	bubble frequency
K	area of influence
k_l	thermal conductivity of liquid
m	mass
n_b	Nucleation site density
q	heat flux
R	distance between the centroids of the bubble and tube
r_b	radius of a bubble
T	temperature
t_d	departure time
t_l	lift-off time
t_w	waiting time
U_b	velocity of the bubble centroid
U_{bulk}	bulk liquid velocity
U_l	local liquid velocity around a bubble
U_r	velocity of the bubble centroid in r-direction
V_b	volume of a bubble
W	linear interpolation weight factor
α	upstream contact angle
α_θ	angular acceleration
β	downstream contact angle
θ_0	angle of the nucleation site
θ_b	angle of the surface normal to the gravitational direction
ρ	density
σ	surface tension
χ_s	parameter defined by the projected area and nucleation site density for sliding bubbles
χ_{st}	parameter defined by the projected area and nucleation site density for stationary bubbles
ω_b	bubble angular velocity

Subscript

b	bubble
l	liquid
me	microlayer evaporation (due to stationary bubble)
mes	microlayer evaporation (due to sliding bubble)
nc	natural convection
v	vapour
tc	transient conduction (due to stationary bubble)
tcs	transient conduction (due to sliding bubble)
tot	total

tubes of the heat exchanger, which generates vapour bubbles on their outer surfaces.

The bubbles generated on the horizontal tube display different characteristics depending on the generation location, as shown in Fig. 2. The bubbles on the upper part of the tube detach from the surface, which is predominantly analogous to a pool boiling on a horizontal plate. However, bubbles on the lower part slide along the downward-facing heated surface after detachment and grow as they slide until they lift off from the surface. This characteristic of the bubble behaviour directly affects the boiling heat transfer. Thus, a mechanistic boiling model with a detailed heat transfer mechanism for boiling is needed to consider the bubble sliding motion. The sliding bubbles on the downward-facing heated

surface appear not only on the horizontal heat exchanger tubes but also in other safety systems of nuclear reactors, such as the IVR-ERVCS (In-Vessel Retention of molten corium through External Reactor Vessel Cooling) [3], core catchers [4], and isolation condenser [5]. In this context, studying the sliding motion along a downward-facing heated surface is an important part of developing an enhanced boiling model applicable to safety systems. Accordingly, models that consider this phenomenon have been proposed in previous studies [6–9].

Boiling models for analysing the heat transfer rate can be classified into classical and mechanistic models. The former is developed by regressing experimental results with respect to various conditional parameters, and the latter incorporates each mechanism that reflects the boiling heat transfer principle. Examples of classical correlations include those by Chen [10], Kutateladze [11], Polley et al. [12], Singh et al. [13], Hwang and Yao [14], and Webb and Gupte [15]. Most of the widely used classical nucleate boiling correlations are based on Chen's model [10], which was developed for the flow boiling in a vertical tube and calculated from the sum of the single-phase convection heat transfer and two-phase boiling heat transfer. Although many researchers have improved upon this model according to various geometries, fluid, and flow conditions, their work has been limited in that they could not directly reflect the detailed mechanism of the boiling heat transfer and relied on empirical fitting to experimental data.

The heat-partitioning model is a mechanistic model and can directly reflect the mechanism of vapour bubble generation and actual phenomena. Researchers have been especially attracted by the extensibility of the model since it was first proposed by Kural and Podowski [16]. In this model, the boiling heat transfer can be calculated from bubble-related parameters such as the volume, velocity, frequency, and other influencing factors. Because of these advantages, it is currently widely used for predicting boiling heat transfer in computational fluid dynamics (CFD) codes. The model has been continuously improved by different groups such as Sateesh et al. [6], Basu et al. [7], Yeoh et al. [8], and Gilman and Baglietto [9]. As an example, the heat-partitioning model proposed by Sateesh et al. [6] for a horizontal tube is given below:

$$q_{tot} = (q_{me} + q_{tc})\chi_{st} + (q_{mes} + q_{tcs})\chi_s + q_{nc}, \quad (1)$$

where q_{tot} is the total heat flux, q_{me} is the heat flux due to microlayer evaporation for stationary bubbles, q_{tc} is the heat flux due to transient conduction for stationary bubbles,

q_{mes} is the heat flux due to microlayer evaporation for sliding bubbles, q_{tcs} is the heat flux due to transient conduction for sliding bubbles, q_{nc} is the heat flux due to natural convection, χ_{st} is a parameter defined by the projected area and nucleation site density for stationary bubbles, and χ_s is a parameter defined by the projected area, nucleation site density, and χ_{st} for sliding bubbles.

The model includes microlayer evaporation and transient conduction for both stationary bubbles and sliding bubbles. In order to apply a heat-partitioning model accurately, parameters associated with the bubble motion such as the bubble velocity and bubble volume (or bubble radius) are of great importance. For example, the transient conduction of sliding bubbles q_{tcs} in Eq. (1) can be expressed with the following sub-model:

$$q_{tcs} = 2 \sqrt{\frac{k_l \rho_l C_{pl}}{\pi t_w} \Delta T n_b t_w f \int_{t_d}^{t_l} K 2 r_b(t) U_b(t) dt}, \quad (2)$$

where U_b and r_b are the bubble velocity and bubble radius, respectively. Eq. (2) represents the transient conduction, and the terms directly include the velocity and radius of a sliding bubble. In addition to Eq. (2), the bubble radius and velocity during sliding are included in the remaining terms of Eq. (1) and are important factors for predicting the total heat transfer.

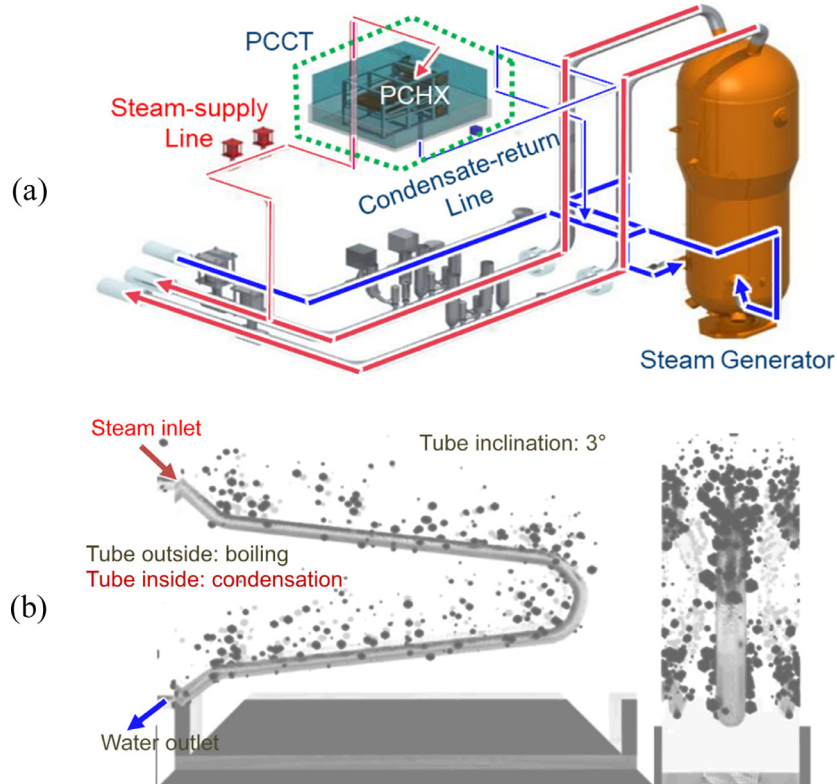


Fig. 1. Passive auxiliary feedwater system and illustration of boiling phenomena: (a) PAFS system configuration [2] and (b) boiling heat transfer on the heat exchanger tube.

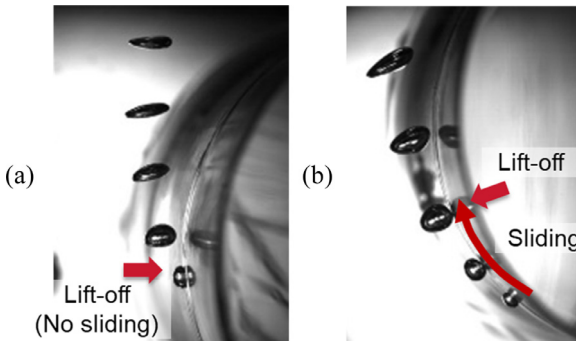


Fig. 2. Different bubble movements on the horizontal tube: (a) upper half and (b) lower half.

Klausner et al. [17] proposed a force balance model that can calculate the forces acting on bubbles and subsequently predict the velocity, bubble departure, and lift-off. Their model has been modified by many researchers since then [18–20] in order to expand its coverage and apply it as a sub-model for heat partitioning. However, this model was developed for horizontal plates and needs to be adapted for cylindrical coordinates to be applicable to horizontal tubes.

Plessset and Zwick [21], Scriven [22], Zuber [23], Mikic et al. [24], Ünal [25], Yun et al. [19], Colombo and Fairweather [26], and Hoang et al. [27] have all proposed models for predicting the bubble growth and radius. However, these models were mostly developed for upward-facing plate surfaces or vertical tubes. Although Maity [28] and Qiu and Dhir [29] studied boiling heat transfer on downward-facing inclined planes, they did not consider the curvature effect of a horizontal tube. Sateesh et al. [6] considered the curvature effect and sliding of bubbles when modelling boil-

ing heat transfer for a horizontal tube. However, their sub-models rely on a simplified analysis of the sliding bubble motion rather than on experimental data. In this context, appropriate sub-models explicitly applicable to horizontal tube boiling have not yet been proposed.

The main objectives of the present work were to examine the sliding bubble behaviour outside a horizontal tube in a visualisation experiment and to establish a force balance model for predicting the sliding bubble velocity. A series of experiments was conducted to observe the bubble behaviour under boiling conditions on the lower surface of a horizontal tube. A specially devised heater was fabricated for this purpose and boiling bubbles were generated along a thin heated surface to facilitate observation of a single bubble's motion. By taking advantage of bubble incipience in the controlled area, accurate measurement of the bubble motion became feasible along with a digital image processing technique. A force balance model was derived to predict the sliding bubble velocity, where the curvature effect was included in an existing force balance model and cylindrical coordinates were adopted. The force balance formula was validated by comparison of the predicted bubble velocity with the experimental data. This paper presents experimental techniques and measurement results for observing vapour bubble sliding phenomena, deriving the force balance equation, and the application of the equation to bubble sliding motion analysis.

2. Experimental setup

As shown in Eq. (2), the bubble sliding velocity and radius (or volume) were required to develop sub-models of the heat partitioning. These parameters were measured at the lower part of a horizontal tube. Fig. 3 shows the experimental loop, which included a water tank, pump, preheater, test section, and heat exchanger connected to a chiller. The water in the water tank was

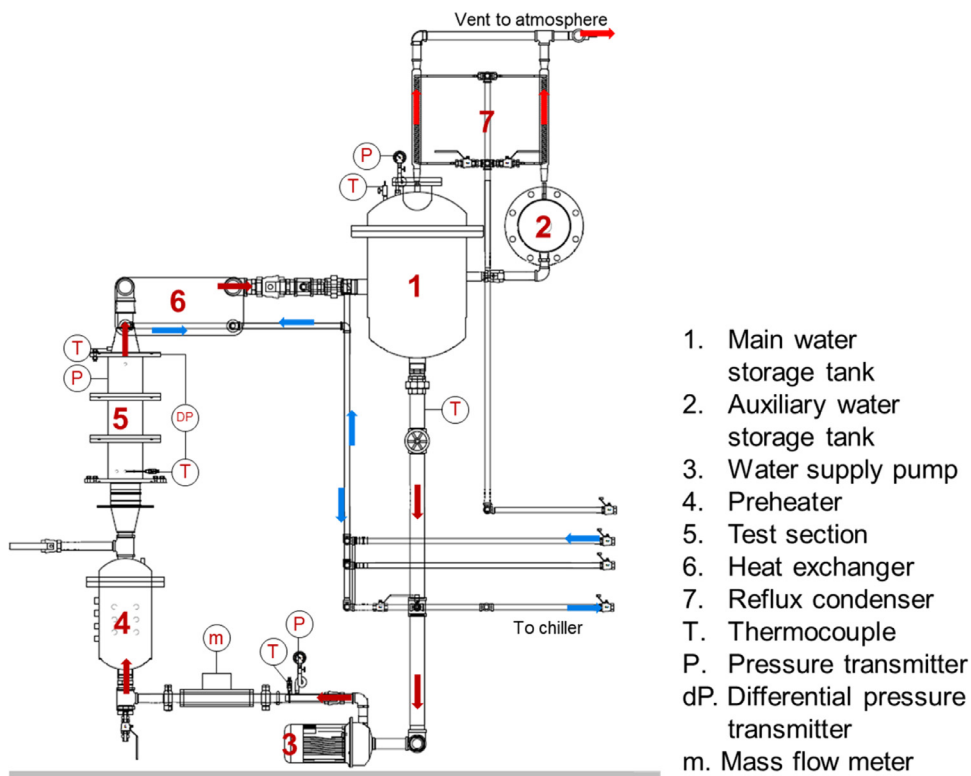


Fig. 3. Schematic of the experiment loop.

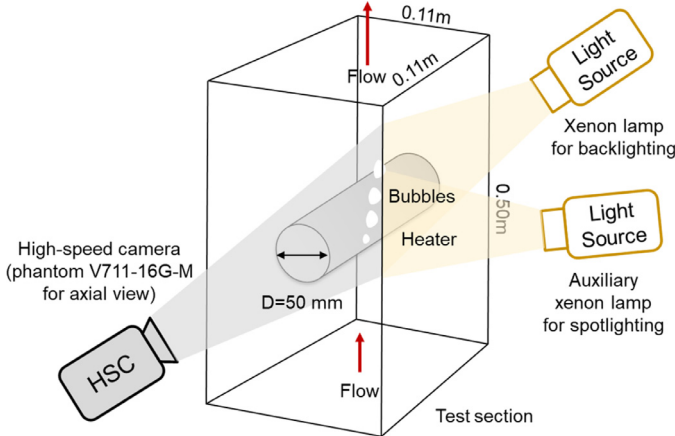


Fig. 4. Schematic diagram of the test section and setup for the visualisation system.

supplied by the pump and heated to the saturation temperature by the preheater. The saturated water was boiled through the heater installed inside the test section. The heat exchanger was installed at the exit of the test section to condense the vapour bubbles, creating a subcooled liquid. The cooled water was transferred to the water tank for circulation. The preheater was used for boiling for more than 2 h before the experiment to deaerate dissolved non-condensable gases.

The shape and size of the test section are shown in Fig. 4. The test section was a $0.11\text{ m} \times 0.11\text{ m}$ transparent square duct made of polycarbonate for visualisation. The test section height was 0.5 m, and a flow straightener was installed at the inlet to flatten the velocity profile. At the middle elevation of the test section, a specially designed heater rod was located with a diameter of 50 mm. The diameter was determined according to the heat exchanger tube diameter of PAFS in APR+ [1]. A conventional car-

tridge heater was not suitable for the present experiment; applying one would generate bubbles on the overall heated surface, and the overlapping bubbles would interrupt the visualisation of important bubble behaviour along the curved surface such as the moment of the bubble lift-off. For this reason, a flexible heater was fabricated with a heating width of 3.0 mm and attached to a polycarbonate rod, as shown in Fig. 5. Fig. 6 depicts the internal structure of the flexible heater. The surface of the heater had a small dent with a diameter of approximately 100 μm to create an artificial cavity where bubbles would be generated. The surface of the heating area was covered with a polyimide layer. The roughness of a polyimide surface ranges from 12 to 35 nm [30] with a contact angle of 73.8–76.9° [31,32]. Because the devised heater generated bubbles on the controlled area, bubbles were generated along the narrow strip. This enhanced visualisation of the bubble motion by avoiding overlap. This feature allowed bubble parameters to be measured through visualisation along the heater rod axial direction, including the bubble contact length and moment of bubble lift-off as exemplified in Fig. 2.

The experiments were carried out at a heat flux of 26–30 kW/m^2 and flow rate of 0.015–0.028 m/s (0.17–0.32 kg/s) to mimic natural convection [1]. The inlet Reynolds number was between 4280 and 10,890. A stagnant flow condition was not included in the experiment because a stabilized condition could not be achieved. However, the conditions with flow rates are more realistic as the natural circulation flow rate exists in the cooling water tank in the prototypic passive safety system. The experimental cases were selected only if consecutive single bubbles were generated on the controlled heating area; this satisfied the study objective of investigating the bubble volume and velocity excluding the bubble coalescence while bubbles slide. The test section was at atmospheric pressure and the corresponding saturation temperature. The tests were performed with two locations for the artificial nucleation site: 23° and 45° from the bottom of the heater rod. The experimental conditions are summarised in Table 1.

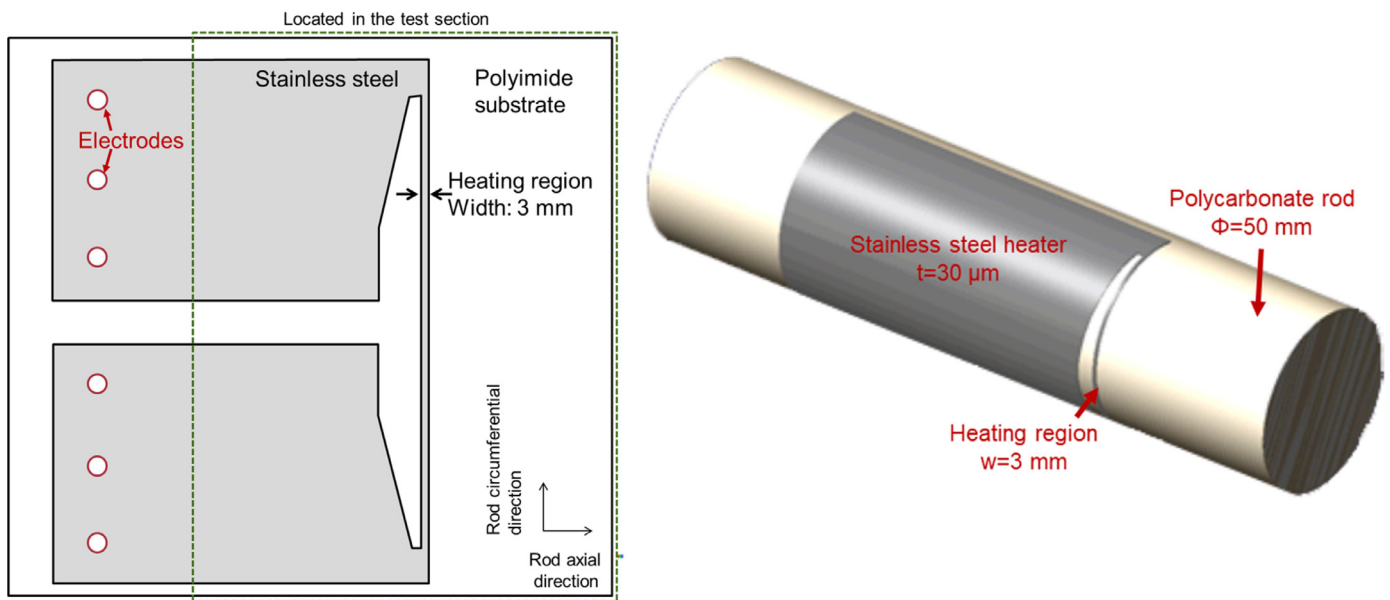


Fig. 5. Schematic diagram of the heater attached to the rod.

Table 1
Test matrix.

Nucleation site angle	23°	45°			
Mass flow rate	0.13 kg/s	0.26 kg/s	0.32 kg/s	0.13 kg/s	0.26 kg/s
Wall heat flux	26 kW/m ² Q26M13A23 30 kW/m ² Q30M13A23	Q26M26A23 Q30M26A23	Q26M32A23 Q30M32A23	Q26M13A45 Q30M13A45	Q26M26A45 Q30M26A45*) Q30M32A45

* Only bubble frequency was measured due to frequent bubble merge.

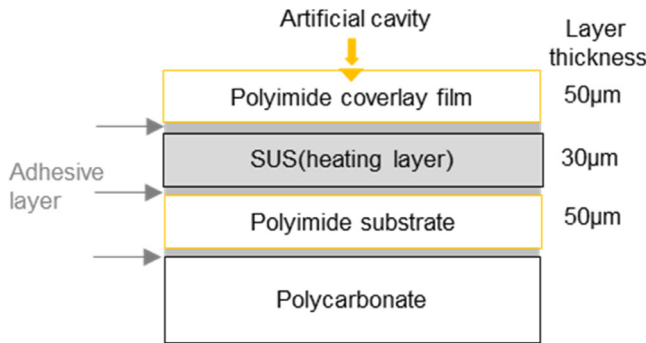


Fig. 6. Schematic of the heater layer.

The measurement parameters of the experiment are shown in Fig. 3. The flow rate was measured by a Coriolis flowmeter (RHM-17,498, Rheonik) with a measurement range of 0–4.17 kg/s and measurement error of less than $\pm 0.3\%$. The pressure was measured by a Rosemount 2051CG with $a \pm 0.01\%$ span error, and the differential pressure between the inlet and outlet of the test section was measured by a Rosemount 2051CD with $\pm 0.02\%$ span error. T-type thermocouples manufactured by Omega were used to measure the liquid temperature with a measurement error of $\pm 1^\circ\text{C}$. The thermocouples were installed in the water storage tank, pump inlet and outlet, preheater chamber, test section inlet and outlet, and downstream of the heat exchanger, as indicated in Fig. 3. The measurement results were collected with a data acquisition system (NI9211, National Instruments).

The bubble parameters of the experiment were measured with a digital image processing technique. Each experimental condition was photographed for 5 s. During this time, 90–320 bub-

bles were photographed depending on the conditions. The volume and velocity of the bubbles were averaged for the data acquisition duration to derive representative values for a specific condition. The images were acquired at 1000 fps from shadowgraphs using a high-speed camera (Phantom V711-16G-M) and backlighting. The acquired images were binarised and analysed to measure the bubble volume and velocity. The image processing procedure is described in detail in the authors' previous study [33]; Fig. 7(a) shows the simplified sequence of the image processing. The procedure includes background image subtraction, binarisation, hole filling, edge smoothening, and verification. In the previous study, a pair of bubble images was recorded simultaneously with two synchronised high-speed cameras (Fig. 7(b)): one in the rod radial direction and the other in the rod axial direction. Then, a three-dimensional volume reconstruction method was applied to evaluate the bubble volume. Based on the experimental data, the relation between the volume from the stereoscopic method and from a conventional monoscopic method was established under various flow and heat flux conditions (Fig. 7(c)). The results indicated that the volume obtained with one camera in the axial direction was $-30\%-0\%$ less than the volume obtained with the stereoscopic method. The reason for the underestimation is the bubble deformation pattern. In the monoscopic method, a horizontal cross-section of the bubble was assumed to have a circular shape. But the bubble volume is large and accelerated, it can be significantly deformed and have an ellipsoidal shape. Especially, the major axis of the ellipsoid is tilted from the horizon as the bubble moves along the circumferential direction of the horizontal heater. Owing to this, the volume estimated using the monoscopic method shows a significant variation with respect to the visualization direction. The views along the heater axial direction caused underestimation of the bubble volume and the other caused overestimation. In the present study, the database from the previous study

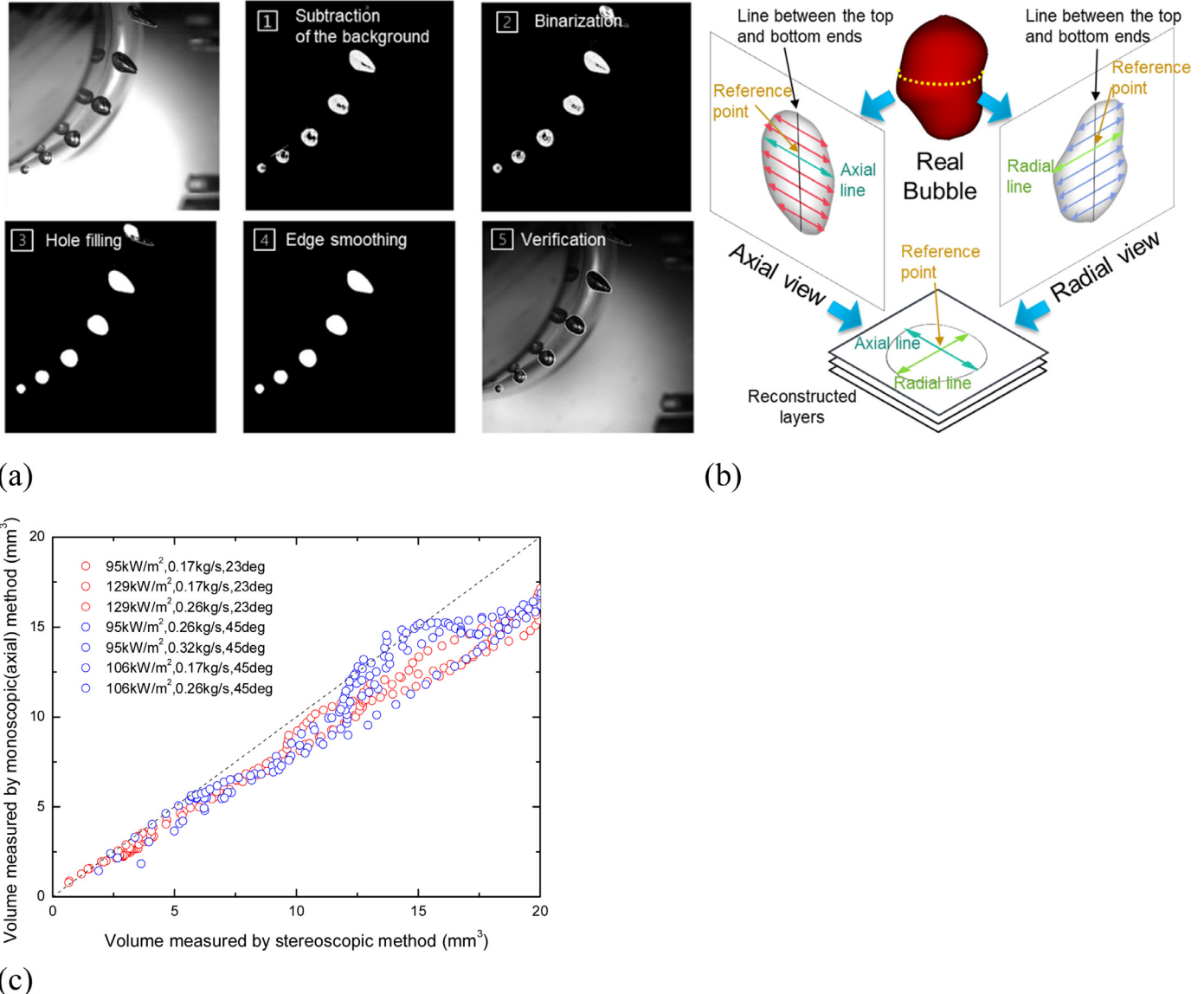


Fig. 7. Image processing procedure and volume reconstruction method from Kim et al. [33]: (a) Image processing procedure (b) volume reconstruction method and (c) Comparison result of bubble volumes between the monoscopic and stereoscopic method.

was applied to evaluate the bubble volume from images obtained from the camera in the rod axial direction. This compensated for non-spherical bubble shapes in the bubble volume evaluation. The uncertainties of the measured bubble parameters were analysed by combining the bias errors and precision errors. For the bubble volume measurement, the sources of uncertainty considered were (i) camera resolution ($\pm 13.87 \mu\text{m}$), (ii) volume compensation for monoscopic method ($\pm 15\%$ volume compensation error of the final volume result) and (iii) the precision uncertainty (Max. $\pm 2.3 \text{ mm}^3$). For the bubble velocity measurement, the uncertainty sources below were considered; (i) camera resolution ($\pm 2.36 \cdot 10^{-3} \text{ m/s}$), and (ii) the precision uncertainty (Max. $\pm 0.032 \text{ m/s}$). These were included in the final measurement results and their error bars.

3. Experimental results

In the present experiment, the bubble velocity and the bubble volume were measured as the main parameters. among the experimental data, cases where bubble coalescence with the preceding bubble did not occur were collected with a focus on single bubble

behaviour. Fig. 8 exemplifies the life cycles of a bubble visualised at two different bubble nucleation sites, including the birth, departure, sliding, and lift-off. If the bubbles appeared to be completely separated from the heated surface in the images, the moment was defined as the bubble lift-off. Fig. 9 shows examples of the measured bubble volume and contact length over time under experimental conditions corresponding to those for Fig. 8. The contact length was the length of the wall surface area in contact with the bubble including the microlayer. The bubble volume increased over time as heat was continuously added. The volume of a bubble increased nearly linearly as it slid; the increasing trend decelerated before lift-off because the contact area of the bubble was significantly reduced during the lift-off process. The bubbles generated at the 23° nucleation site had a greater sliding length, which increased the bubble volume at lift-off. The bubbles at 45° showed a slightly greater rate of increase in the volume, but the contact length seemed shorter. This implies a faster bubble growth rate with a smaller heat transfer area between the wall and bubble. This can be explained by the enthalpy in the superheated liquid layer near the nucleation site. The enthalpy of the liquid increased

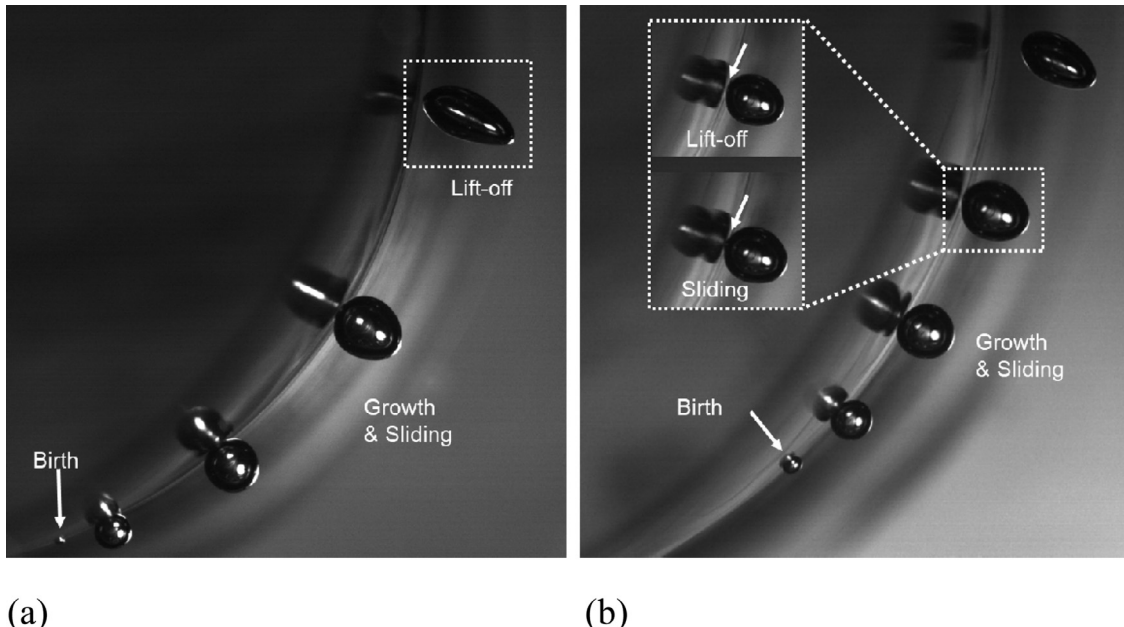


Fig. 8. Life cycles of a bubble: (a) Q26M13A23 and (b) Q26M13A45.

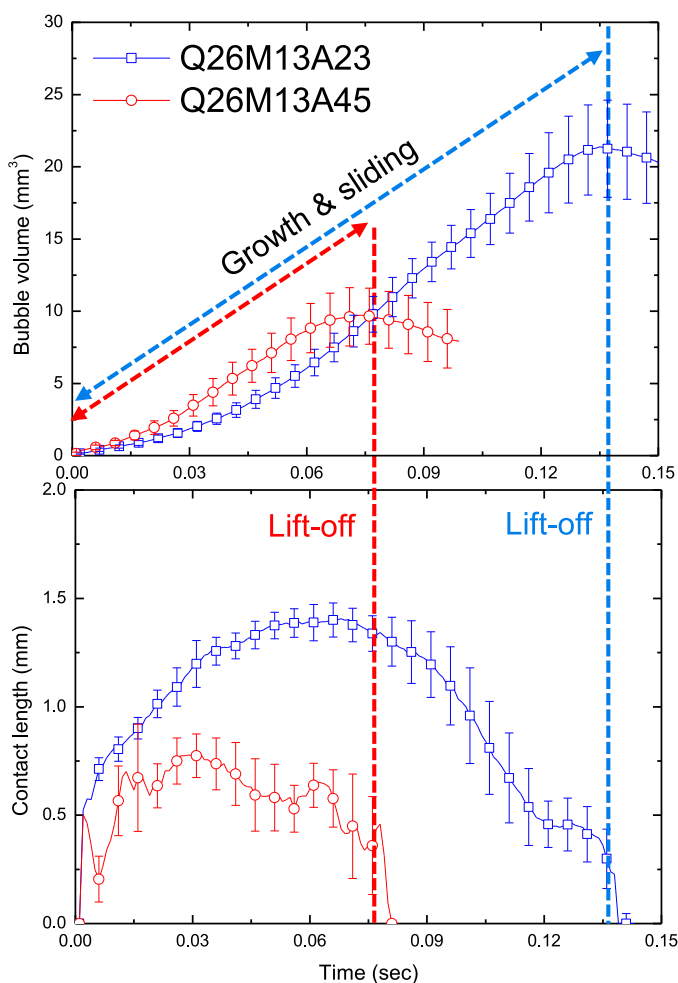


Fig. 9. Bubble volume and contact length transient in the bubble life cycle.

from the bottom end of the heated surface to the nucleation site. Because the 45° case had a greater heating length upstream of the nucleation site, more energy was accumulated in the liquid. Thus, when nucleation started, the bubble in the 45° case had a faster growth rate.

Figs. 10 and 11 show the experimental results for the bubble volume under different conditions, and Fig. 12 shows the bubble frequency (number of bubbles generated per second) with respect to the liquid mass flow rate. The results showed a clear tendency of the wall heat flux effect on the bubble growth rate. The comparison between Fig. 10(a) and (b) and Fig. 11(a) and (b) show that the rate of volume increase was lower at a higher heat flux. Under higher heat flux conditions, bubbles were more frequently generated as shown in Fig. 12. This decreased the bubble waiting time, which induced a lower liquid enthalpy that accumulated along the bubble sliding path. This effect lowered the growth rate of the sliding bubble at a higher heat flux.

The effect of the liquid flow rate on the bubble growth rate is rather indistinctive. As shown in Figs. 10 and 11, the volumes of the vapour bubbles increased over time with similar growth rates regardless of the flow rate early in the bubble history. This implies that the liquid velocity near the wall had an insignificant influence on the bubble growth rate during this time period. As the bubbles accelerated, the growth rate varied with it slightly. Depending on the bubble frequency trend along the liquid flow rate, however, the growth rate trend was changed. In principle, the bubble receives higher drag force with increased relative velocity and this causes more frequent bubble departure from the surface and the increased bubble departure frequency. When the bubble frequency has the increasing trend along the mass flow rate (Q30A23 and Q30A45 in Fig 12), the volume increasing rate was decreased with the flow rate. It is correspondent with the heat flux effect described in the paragraph above. On the other hand, when the wall heat flux is small (Q26A23 and Q26A45 in Fig 12), it was difficult to find a clear tendency between the bubble frequency and the flow rate due to the large fluctuations in the bubble frequency. Under these conditions, the effect of the liquid flow rate showed the indistinctive tendency. These experimental results showed that the bubble growth rate is more dominantly influenced by the bubble frequency than the liquid flow rate.

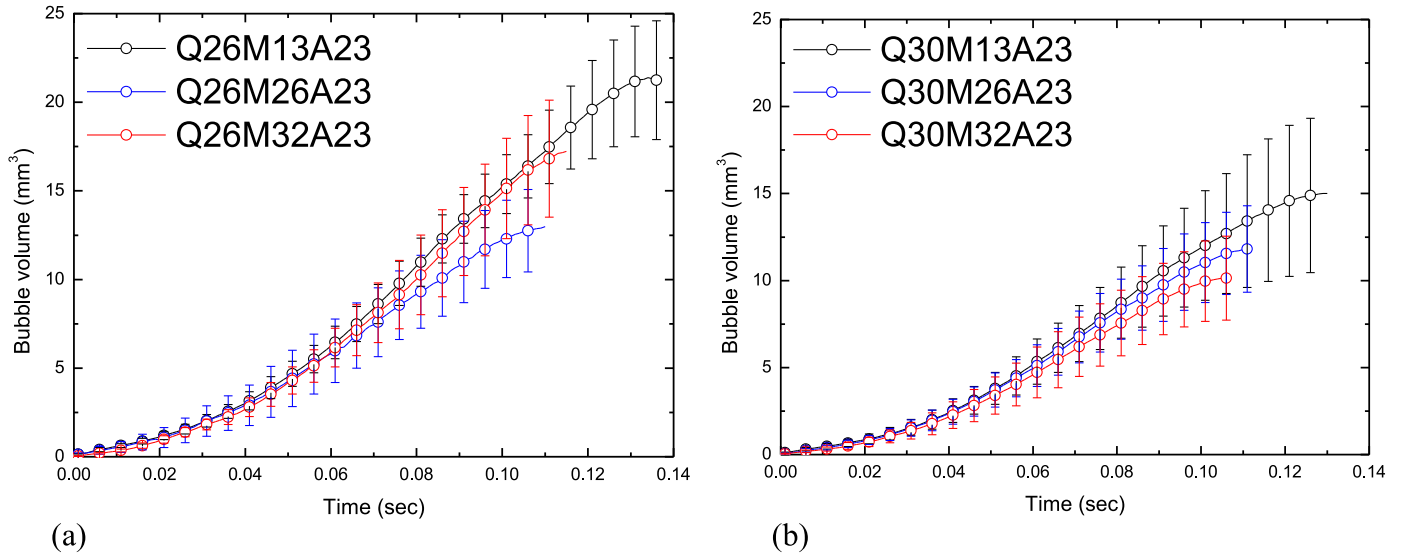


Fig. 10. Experimental results for the bubble volume over time: (a) Q26A23 and (b) Q30A23.

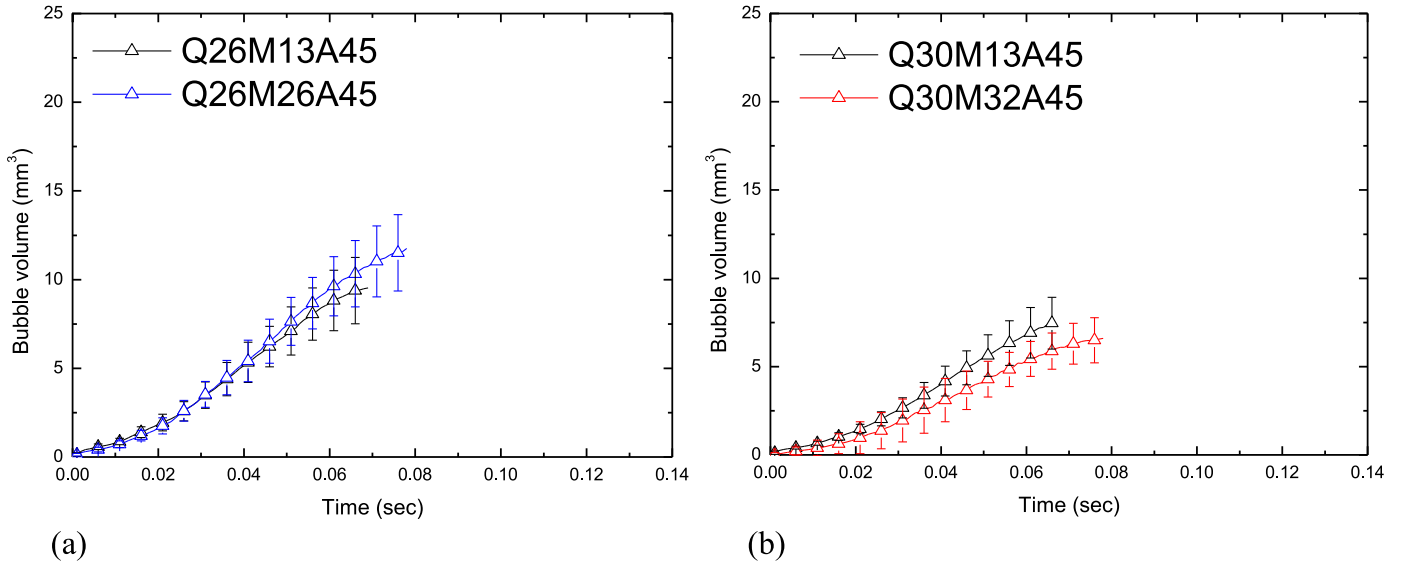


Fig. 11. Experimental results for the bubble volume over time: (a) Q26A45 and (b) Q30A45.

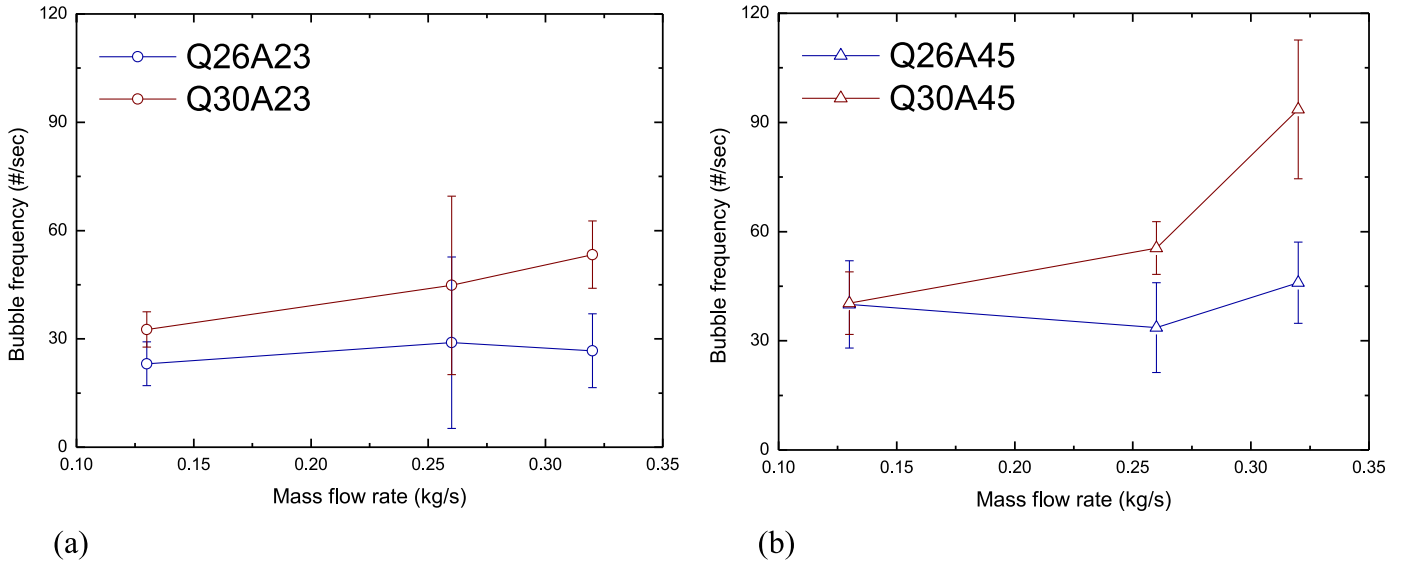


Fig. 12. Bubble frequency by inlet mass flow rate: (a) nucleation site at 23° and (b) nucleation site at 45°.

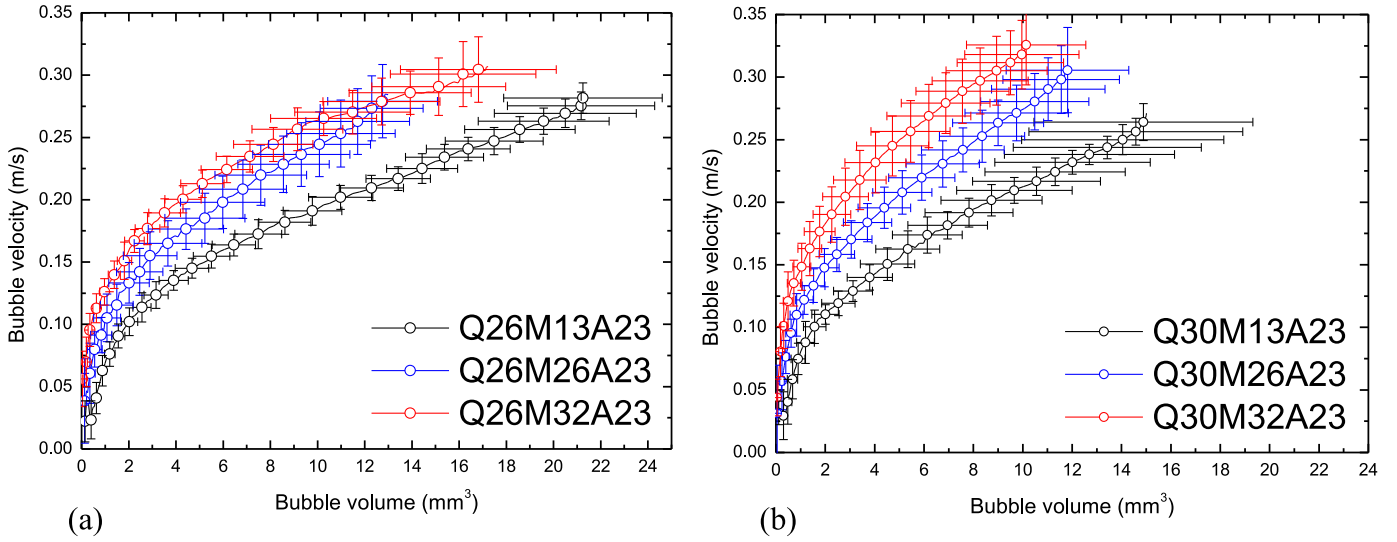


Fig. 13. Experimental results for the bubble velocity by bubble volume: (a) Q26A23 and (b) Q30A23.

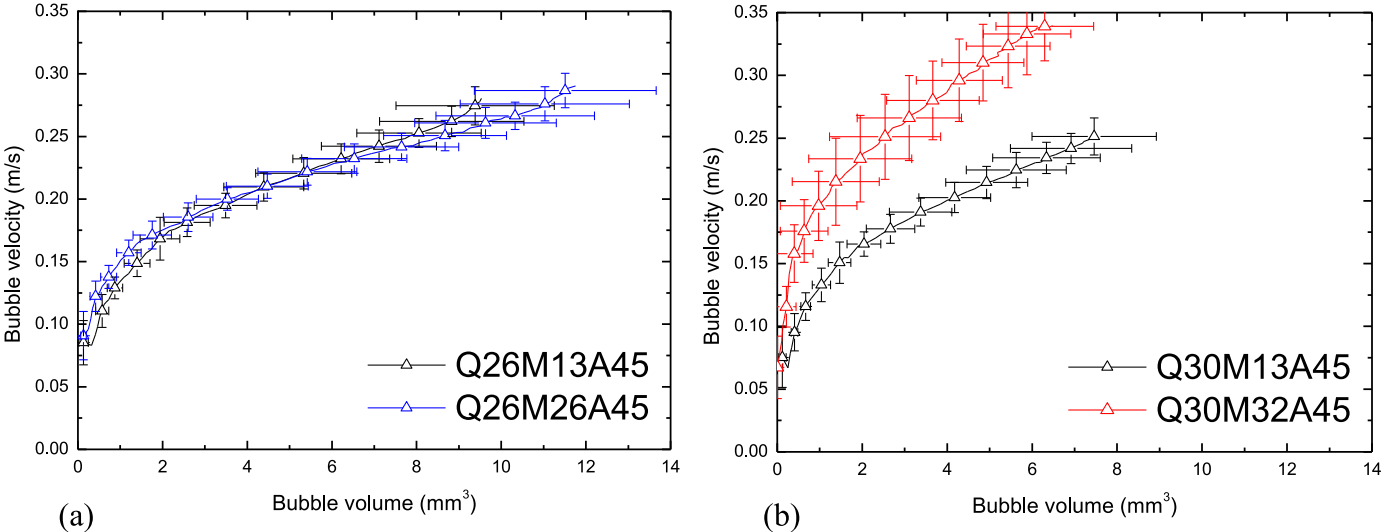


Fig. 14. Experimental results for the bubble velocity by bubble volume: (a) Q26A45 (b) Q30A45.

In addition, an effect of the nucleation site location and the angle of heating surface appeared in Fig. 12. In this study, the experiment was conducted using a single bubble generation (nucleation) site. Therefore, the amount of liquid enthalpy accumulated from 0 to 45° is larger than the accumulated amount from 0 to 23° . This accumulated liquid enthalpy influences the bubble generation rate. The bubbles generated at 45° grow faster than those at 23° resulting in faster departures and higher frequencies. In addition, the bubbles generated at 45° receive a higher buoyancy force because of the steeper heating surface angle. It may also contribute to the higher departure frequency of the bubbles generated at 45° .

Figs. 13 and 14 show the bubble velocity with respect to the bubble volume. As a bubble slid, its volume increased because of the supplied heat, which caused the bubble to accelerate owing to the buoyancy force. Because of the geometric characteristics of the horizontal tube, where the direction of the surface tangential vector varied continuously, the bubble velocity continuously increased from the bubble generation to lift-off without reaching a specific terminal velocity. Even at the same bubble volume, the bubble velocity varied with the external flow rate. A higher bubble velocity was obtained with a higher liquid flow

rate, so it was obviously affected by the drag force. Meanwhile, the rate of increasing bubble velocity when the bubble volume was less than 0.5 mm^3 was related to the bubble frequency. At a higher bubble frequency (e.g. Q30M32A45 in Fig. 14), the rate of increase in the bubble velocity with respect to the volume appeared to be much higher. This phenomenon may be the effect of the preceding bubble on the trailing bubble. At a high bubble frequency, the wake of the preceding bubble may effectively accelerate the trailing bubble and result in a faster bubble velocity. As shown in Fig. 12, cases with a high flow rate had a significantly greater bubble frequency than those with low mass flow rates. This implies that the preceding bubble effect needs to be considered to accurately predict the bubble velocity with the force balance model.

4. Force balance in the θ direction

A force balance analysis was performed to evaluate the velocity of the bubble and forces acting on it based on the experimental data. Klausner's force balance model was modified to adopt the $r-\theta$ coordinate system to accommodate the horizontal tube condition. The bubble acceleration vector of circular motion is expressed as

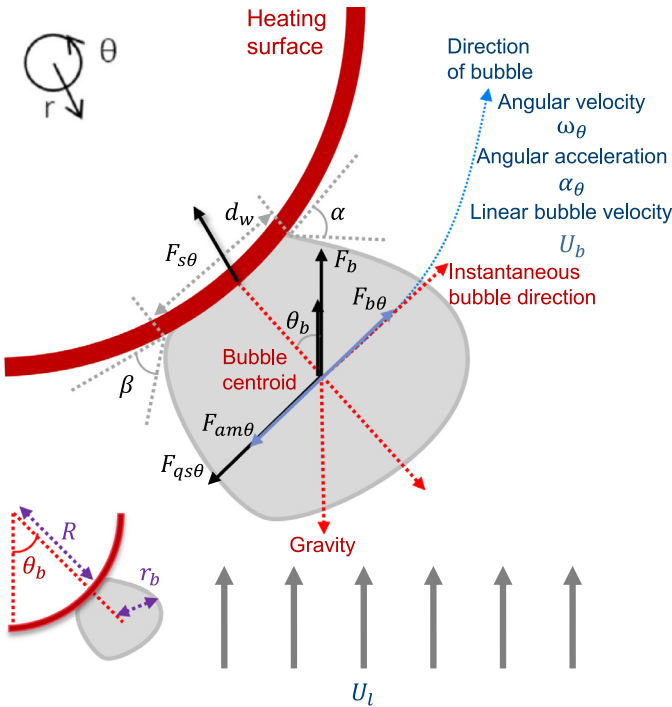


Fig. 15. Forces acting on the bubble in the θ direction.

angular acceleration of $r-\theta$ coordinates system, and the circumferential acceleration components in the θ -directions is Eq. (3) In this study, the force acting in the θ direction (circumferential direction) was analysed; only the circumferential velocity of the bubble as it slid along the heater surface was considered. The r -directional force balance analysis was excluded but is described in a previous paper by the authors [33]. The sum of the forces exerted on the bubble in the θ direction is expressed below and includes the buoyancy force, quasi-steady drag force, surface tension force, and added mass (Fig. 15, Table 2).

$$F_{tot,\theta} = F_{b\theta} + F_{qs\theta} + F_{s\theta} + F_{am\theta} \quad (3)$$

$F_{b\theta}$ is the buoyancy force in the θ direction acting on the bubbles. The buoyancy increases with the bubble volume and θ_b (i.e. angle between the surface normal vector and gravitational force). The quasi-steady drag force $F_{qs\theta}$ is the drag force exerted in the θ direction when the bubble is moving at a velocity different from that of the liquid and is calculated from the relative velocities of the external fluid and bubble. The drag force changes with the bubble configuration, but a spherical bubble shape was assumed to simplify the modelling. Based on this assumption, the bubble cross-sectional area (A) and bubble resistance coefficient (C_D) were determined as listed in Table 2. To evaluate the drag force, the liquid velocity was required. In the force balance analyses of previ-

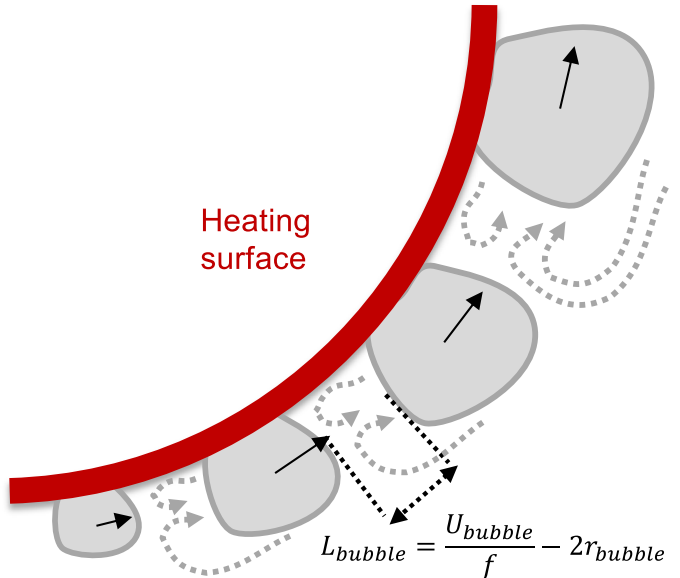


Fig. 16. Increase in the local liquid velocity with continuous bubbles.

ous studies, the local liquid velocity was assumed to be the same as the bulk velocity [7,9,19] or half of the bulk velocity [35]. In the present study, the former assumption was applied for the drag force evaluation except when the bubble frequency was greater than a certain criterion. According to the insight obtained in the previous section, the bubble velocity notably increased when the bubble frequency was high (Fig. 16). Based on this, it was assumed that the wake effect of the preceding bubble needed to be considered when the gap between two consecutive bubbles was less than the twice of bubble diameter ($L_{bubble} \leq 2D_b$). This assumption is based on the local liquid velocity measurement data using PIV for the sliding air bubbles and the experimental observation was explained in the appendix. At the same time, the liquid velocity was assumed to be the average of the bulk liquid and sliding bubble for the limiting case when two bubbles make a contact ($L_{bubble} = 0$). A linear interpolation was applied between the two boundary values, as given below:

$$\begin{aligned} &\text{when } L_{bubble} = 0, \quad U_l = \frac{U_{bulk} + U_b}{2} = U_{l,0}, \text{ when } 0 < L_{bubble} < 2D_b, \quad U_l = (1 - W) \cdot U_{l,0} + W \cdot U_{bulk}, \quad W = L_{bubble}/2D_b \\ &\text{when } L_{bubble} \geq 2D_b, \quad U_l = U_{bulk}, \end{aligned} \quad (8)$$

where, W is linear interpolation weight factor

With the above assumption, the acceleration of the bubble by a preceding bubble could be considered in the bubble velocity modelling.

The surface tension force $F_{s\theta}$ in the θ direction generated by the portion of the bubble contacting the wall [17,33], the dynamic contact angle, and the area of the bubble contact were required. In this study, the advancing and receding dynamic contact angles

Table 2
Forces acting in the θ direction [33].

Force	Equation	Remarks
Buoyancy force	$F_{b\theta} = (\rho_l - \rho_v)gV_b \sin \theta_b$	(4)
Quasi-steady drag force	$F_{qs\theta} = -\frac{1}{2}C_D\rho_l(U_b - U_l) U_b - U_l A$	(5)
Surface tension force	$F_{s\theta} = -\int_0^\pi d_w \sigma \cos \gamma \cos \phi d\phi \sim d_w \sigma \frac{\pi(\alpha - \beta)}{\pi^2 - (\alpha - \beta)^2} [\sin \alpha + \sin \beta]$	(6)
Added mass force	$F_{am\theta} = -\frac{1}{2}\rho_l V_b a_\theta - 2A\rho_l(U_b - U_l)\dot{r}_b$	(7)

$C_D = 0.44$ [34], $A = (\frac{3}{4}\pi^{1/2}V_b)^{2/3}$ where A was calculated assuming a spherical bubble shape

Mean values of the experimental dynamic contact angle; $\alpha = 45^\circ$, $\beta = 30^\circ$

(α and β , respectively) were obtained based on visual observation and set to 45° and 30° , respectively. The added mass force F_{am} was included as a virtual mass because the surrounding fluid needed to be accelerated for the bubble to progress [36]. In the Eq. (7), the first term in Eq. (7) is the added mass force due to bubble progression, and the second term is the added mass force due to bubble growth as a volume of fluid moved outward following a phase change [36]. However, the added mass force due to bubble growth was negligible compared to that exerted by the surrounding fluid. Because the heat flux is not so large that the second term due to bubble growth is relatively very small.

By integrating Eq. (3) numerically, the bubble acceleration could be evaluated at every time step. The bubble velocity and location could also be evaluated by integrating the acceleration under the initial conditions. The numerical integration of the equation started with the bubble departure volume as the initial condition. When the departure moment was not captured, the diameter and the velocity closest to the bubble departure were set to as the initial conditions. For the integration, the bubble volume, contact diameter, dynamic contact angles, drag coefficient, and liquid velocity were needed. Let $U_{b,i}$ and $\theta_{b,i}$ be the bubble

velocity and position, respectively, at the i th time step. Then, $U_{b,i+1}$ and $\theta_{b,i+1}$ are the bubble velocity and position, respectively, at the $(i + 1)$ th time step after a short time duration (Δt). With the explicit Euler numerical integration, the bubble velocity and location angle can be expressed as follows:

$$U_{b,i+1} = U_{b,i} + a\Delta t, \theta_{b,i+1} = \theta_{b,i} + \frac{U_{b,i}}{R}\Delta t \quad (9)$$

The time step for the force balance analysis was set to 0.001 s to maintain consistency with the time span associated with the frame rate of the high-speed video recording. The measured experimental values of the bubble volume was used for each time step. Because the bubble volume had a dominant effect on the force balance analysis but extant models on the bubble growth rate could not capture the experimental data with acceptable accuracy, the measured bubble volume was directly applied in the analysis with a focus on predicting the bubble velocity with the force balance model. The bubble volumes used for the present analysis can be replaced if a proper model for the bubble growth rate applicable to the present conditions is proposed.

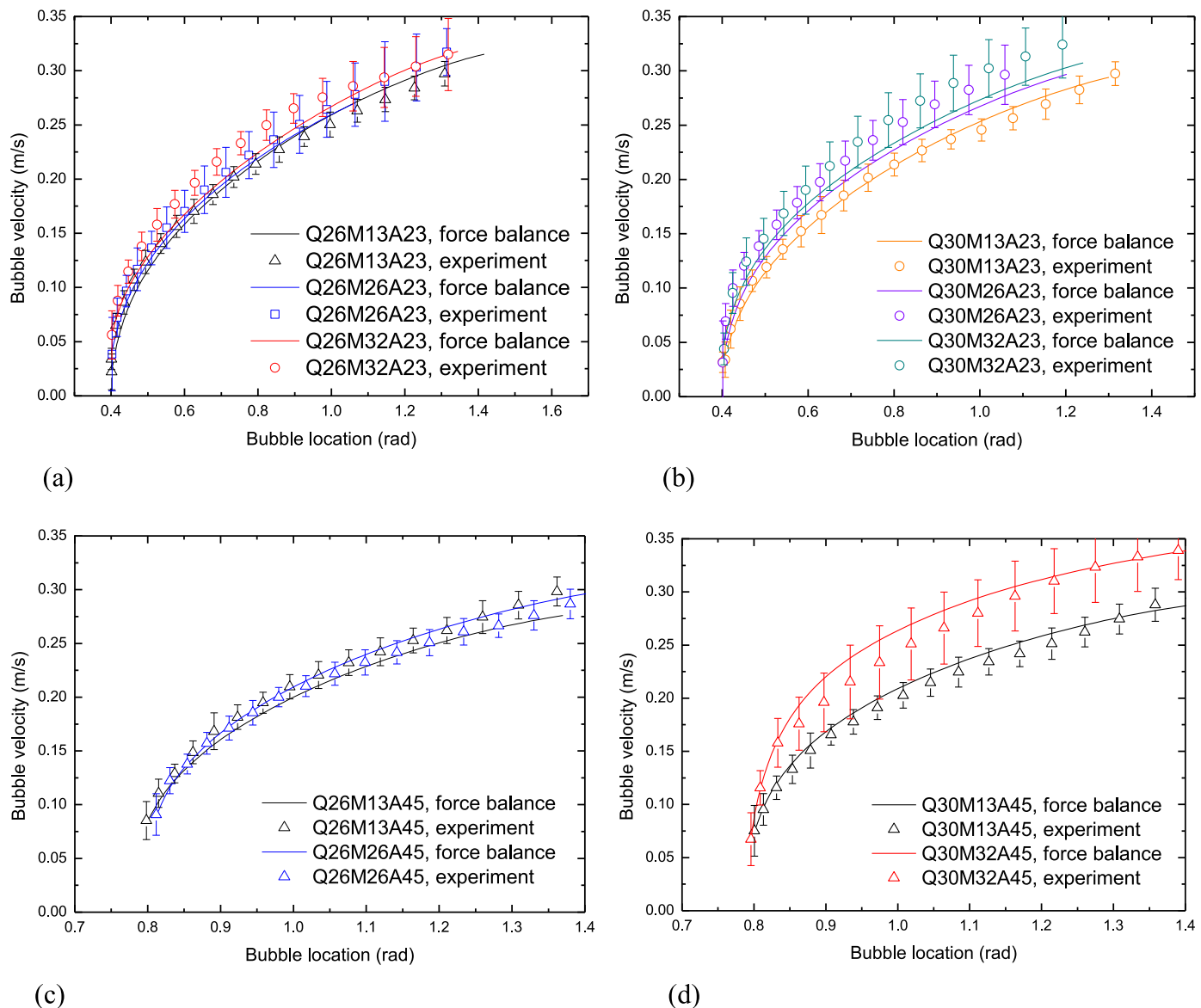


Fig. 17. Bubble velocity along the circumference: (a) Q26A23, (b) Q30A23, (c) Q26A45, and (d) Q30A45.

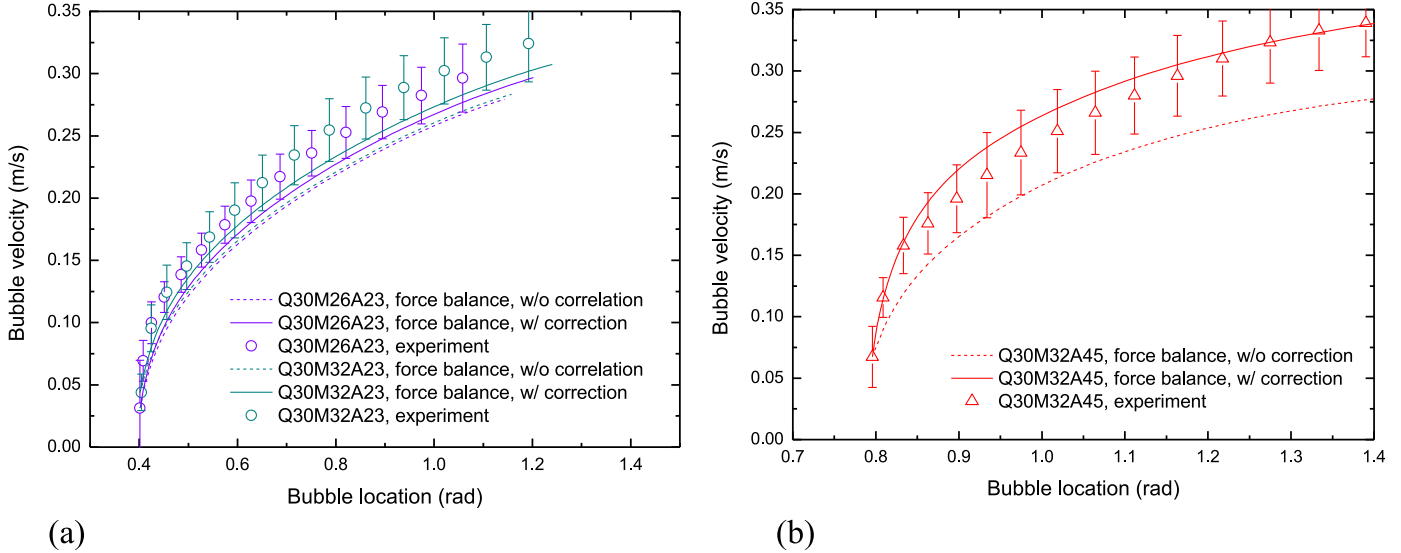


Fig. 18. Bubble velocity along the circumference before and after liquid velocity correction: (a) Q30A23 and (b) Q30A45.

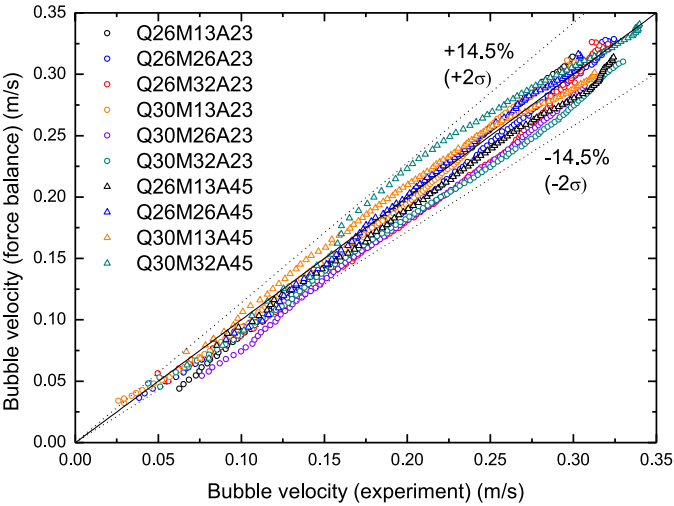


Fig. 19. Estimated bubble velocity.

5. Bubble velocity prediction result

The force balance model described in the previous section was used to predict the bubble velocity in the θ direction. Fig. 17 compares the experimental values for the bubble velocity and the values obtained with the force balance. The experimental results showed that the bubbles accelerated rapidly within a short time after their departure, and the increase in the velocity gradually decelerated as the bubbles slid along the heater wall. Before reaching terminal velocity, the bubbles lifted off the heated surface. This trend was attributed to the continuously changing bubble volume because of evaporation and the varying angle between the gravitational force and wall due to the horizontal tube geometry. The bubble sliding velocity predicted by the force balance model qualitatively reproduced this tendency well. Fig. 18 compares the predicted bubble sliding velocity with and without the liquid velocity correction from Eq. (8) at relatively high bubble frequencies. The force balance model consistently underestimated the bubble velocity without the correction. This clarifies that the local liquid velocity correction is needed to consider the wake generated by the preceding bubble. As shown in Fig. 19, the model predicted the

bubble velocity within an error of about $\pm 14\%$ (2σ) after the correction.

Fig. 20 displays the magnitude of each force obtained from the force balance analysis for two cases. The dominant forces turned out to be the buoyancy, quasi-steady drag, and added mass forces. In the results, the buoyancy force grew rapidly over time because of the increases in the bubble volume and angle of the wall, which increased the gravitational force as the bubble slid. Throughout the period during which bubbles were generated and lifted off, the buoyancy was considered to be the only significant positive directional force in the advancing direction. Because the velocity difference between the bubble and liquid increased with the bubble velocity, the quasi-steady drag increased accordingly. This force acted in the opposite direction of the bubble advancement. At the beginning of the bubble cycle, the magnitude of this force was relatively small, but it occupied most of the opposite directional force as the bubble accelerated. The added mass force acted to decelerate the bubble in the opposite of the sliding direction. It took up 20%–40% of the opposite directional force during the cycle. The surface tension force initially accounted for about 60% of the opposite directional force, but the proportion became relatively small as the bubbles grew and accelerated. This analysis showed that the surface tension force in the θ direction did not have a significant influence on the predicted sliding bubble velocity.

The above force analysis showed that the balance between the drag and gravitational forces played a major role in determining the bubble sliding velocity. The balance between inertia forces such as the drag force and the gravitational force can be represented in dimensionless form with the Froude number. Thus, the experimental data and force balance analysis results are plotted in Fig. 21 with the local Froude number defined as follows:

$$Fr_\theta = \frac{U_{b,\theta} - U_{l,\theta}}{\sqrt{g \cdot r_{b,\theta}}} \quad (10)$$

where θ is the circumferential location of the bubble. The liquid velocity in Eq. (8) was applied to consider the liquid acceleration from the preceding bubble. The Froude number showed a sharp increase immediately after bubble formation. After the bubble departed, the increasing trend decelerated and instead increased rather linearly. The Froude number curves of all cases converged approximately to a single line regardless of the bubble generation location, heat flux, and bulk liquid flow rate. On a horizontal tube surface, instead of reaching the terminal velocity, the

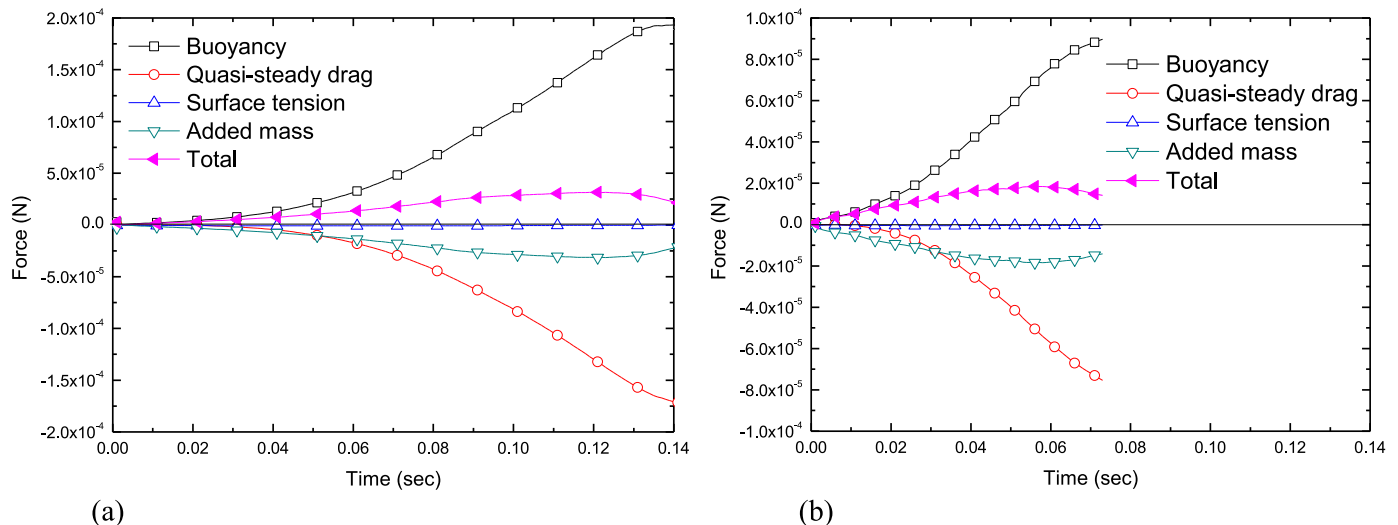


Fig. 20. Force balance analysis results: (a) Q26M13A23 and (b) Q26M13A45.

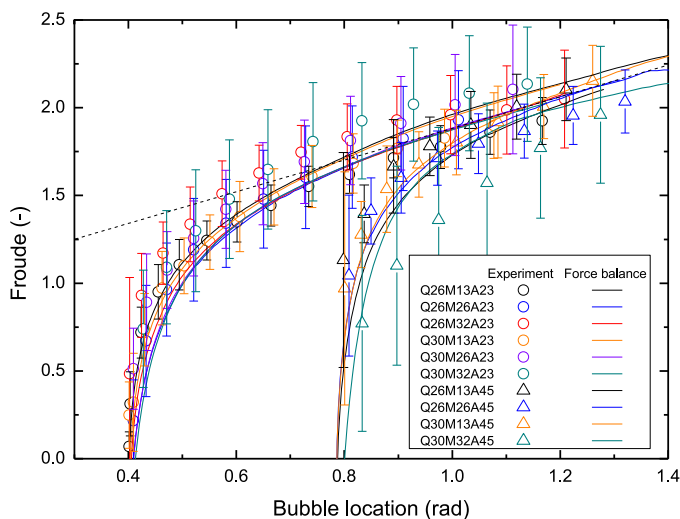


Fig. 21. Froude number according to the bubble position.

sliding bubble velocity seemed to increase according to a constant linear inertia–buoyancy force ratio (Fr). The bubbles continued to increase in radius (or volume) as they slid, which resulted in larger denominator. Also bubble velocity continued to increase because the bubble continuously accelerated by θ directional net force (always positive in this experimental conditions), which resulted in larger numerator. Therefore, the force ratio was non-dimensionalised by the Froude number which contains the bubble velocity and bubble radius. This analysis showed that the sliding bubble velocity correlates well with the bubble location when it is non-dimensionalised with a form of Fr and can be applied as a representative dimensionless number to correlate to the sliding velocity in the heat partitioning model.

6. Conclusion

This study examined the sliding bubble behaviour on the lower surface of a horizontal tube through a visualisation experiment with a digital image processing technique. A force balance model was established for predicting the sliding bubble velocity. An experimental loop and specially devised heater were fabricated to facilitate observation of a single bubble's motion.

The established force balance formula was validated by comparing the predicted bubble velocity with the experimental data. The analysis showed that the dominant forces were the buoyancy, quasi-steady drag, and added mass forces. The surface tension force in the θ direction did not have a significant influence on the predicted sliding bubble velocity. The bubble velocity increased notably when the bubble frequency was high. It was assumed that the wake effect of the preceding bubble needs to be considered. The model predicted the bubble velocity within an error of about $\pm 14\%$ after the correction. Afterward, a method was proposed for expressing the sliding bubble velocity by using the Froude number, which is the ratio between the bubble buoyancy and inertia forces. On a horizontal tube surface, instead of reaching the terminal velocity, the sliding bubble seemed to increase according to a constant linear Froude number with respect to the angular location of the heater.

This study focused on the bubble velocity model based on the θ -directional momentum equation. In order to complete the heat partitioning modelling, models for the bubble lift-off diameter and the sliding length are required for the future work. They can be developed based on the r-directional momentum equation and the lift-off diameter and sliding length database measured in this experiment would be useful for understanding of the phenomena and validation of the models.

Declaration of Competing Interest

The authors declare that they have no known competing financial interests or personal relationships that could have appeared to influence the work reported in this paper.

CRediT authorship contribution statement

Jae Soon Kim: Conceptualization, Methodology, Software, Validation, Formal analysis, Investigation, Data curation, Writing – original draft, Writing – review & editing, Visualization. **Yu-Na Kim:** Conceptualization, Methodology, Software, Formal analysis, Investigation, Data curation. **Hyoung Kyu Cho:** Conceptualization, Methodology, Resources, Writing – original draft, Writing – review & editing, Supervision, Project administration, Funding acquisition.

Acknowledgements

This work was supported by the Nuclear Safety Research Program through the Korea Foundation of Nuclear Safety (KoFONS) and granted financial resources from the [Nuclear Safety and Security Commission](#) (NSSC), Republic of Korea (No. 1307011).

Appendix A. Air bubble-water local liquid velocity experiment

In this study, an additional air bubble PIV test was performed to investigate the local liquid velocity around air bubbles and the fluid field changes around the bubble during the sliding. Based on the experimental results, a simplified assumption for the liquid velocity was proposed to calculate the quasi-steady drag of the force balance model.

In this experiment, the surrounding flow velocity field changes due to the sliding of a single air bubble. For this reason, air bubbles were generated sufficiently slowly so that the flow field was not greatly affected by the preceding bubbles. Working fluid was water and the experiments were carried out at a flow rate of 0.12 kg/s. The test section was at atmospheric pressure and the ambient temperature. The experimental setup is illustrated in Fig. A.1(a).

In the experiment, the bubble images were taken using both PTV and PIV methods; the former for the bubble velocity and the latter for the liquid velocity. The bubble images were analysed in the same way as the phase separation technique described in the [Section 2](#), and the location and velocity were analysed. The contin-

uous light was irradiated for the PIV and fluorescent particles were mixed into the fluid.

A typical result is shown in Fig. A.2(b). In this case, the fluorescent particles emit light of a higher frequency by receiving the laser light, and a high pass filter is installed in front of high speed camera. Through this, wavelengths other than laser light reflected by the fluorescent particles was blocked to increase the accuracy of PIV analysis. For flow field analysis, Insight 4 G, a commercial PIV software, was used. The PIV analysis results are shown in Fig. A.2(c).

Fig. A.3. shows the local liquid velocity over time measured at a specific location, indicated by a white dot where the maximum liquid velocity appears. As the bubble passed through this point, it can be seen that the local liquid velocity was affected. Initially, the velocity of the local liquid maintains the bulk velocity and is not affected by bubbles (Fig. A.3.①). However, as the bubble approached to the sampling point, the liquid in the measurement section began to accelerate (Fig. A.3.②), and immediately after the bubble passed, the local liquid velocity at the position reached its maximum value, which was almost the same as the bubble velocity (Fig. A.3.④). Then, as the bubble moved away and over time, the flow velocity at the measuring point was reduced to its original bulk velocity (Fig. A.3.⑦). This change in local liquid velocity was repeated periodically as the trailing bubble passes.

It should be noted that the liquid velocity right behind the bubble was close to the sliding bubble velocity at the centre location of the bubble. If there are no bubbles, the flow velocity profile

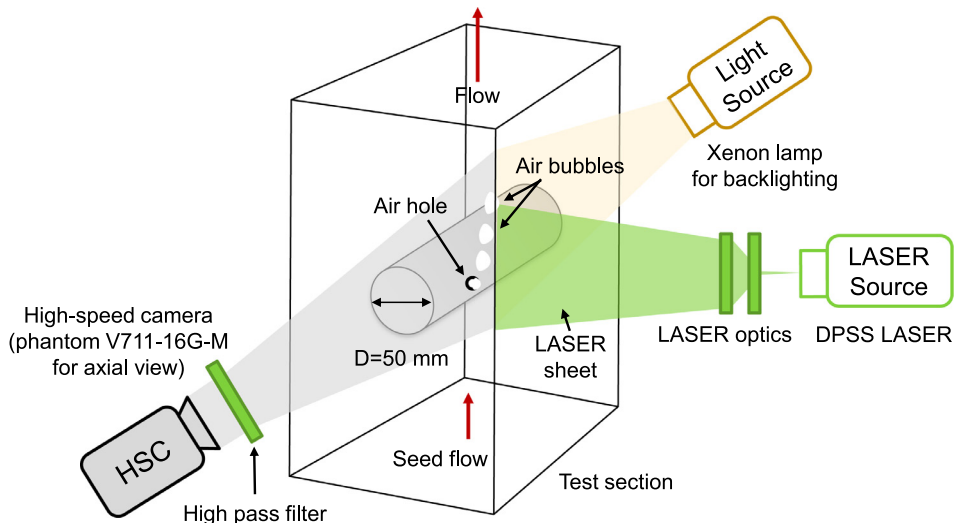


Fig. A1. Schematic diagram of the test section and setup for the PIV, PTV visualisation system.

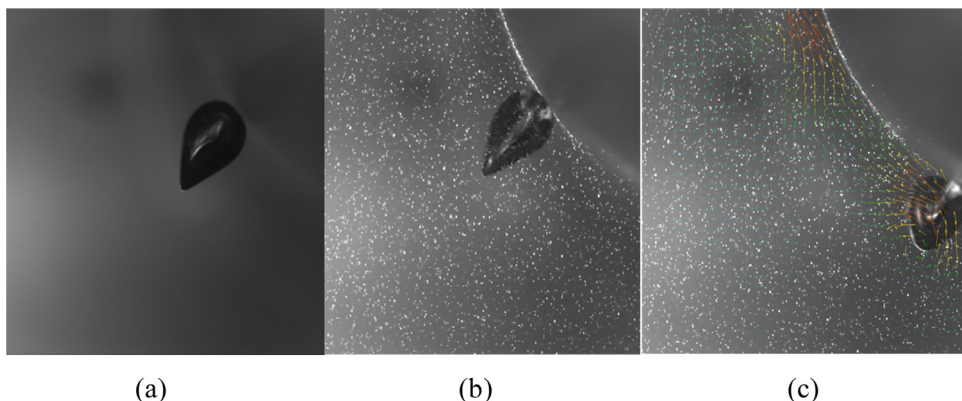


Fig. A2. Image samples of: (a) Bubble image, (b) Bubble image with laser, (c) PIV analysis result.

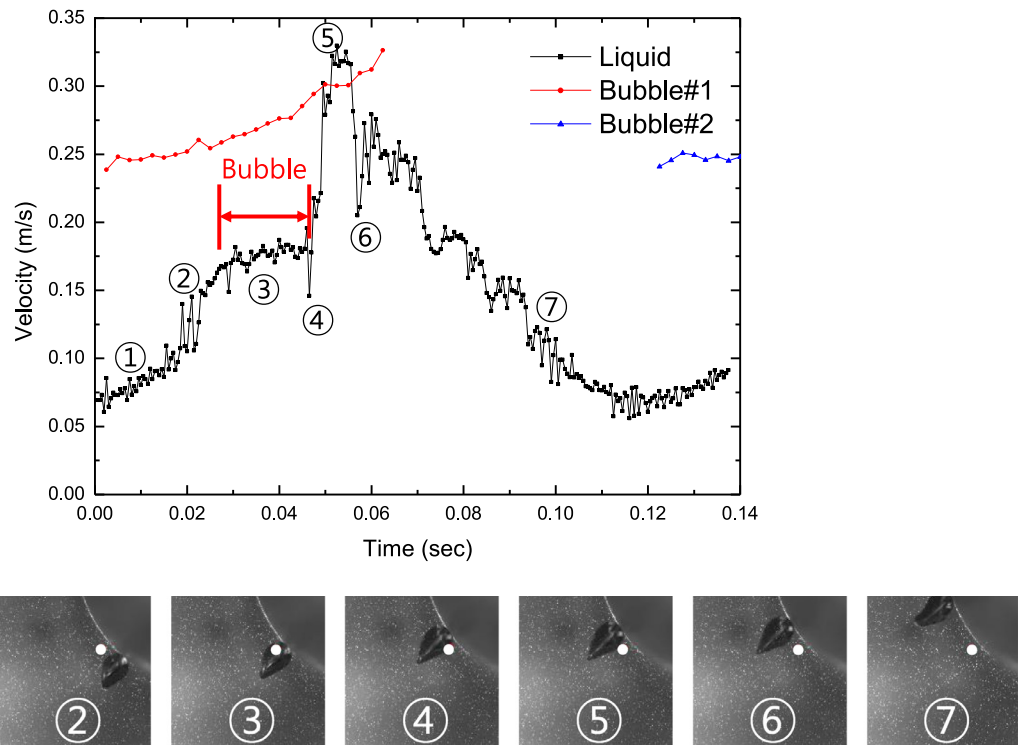


Fig. A3. Local liquid velocity and bubble velocity at the measuring point.

starts from zero on the heater surface and increased to the bulk flow velocity as the distance to the rod surface increases. If bubbles exist, however, the liquid velocity profile approaches to the bubble velocity and then decreases to the bulk velocity (the bubble velocity is faster than the bulk velocity for most of the time except at the very beginning of initial bubble generation under the experimental conditions of this study). Previous studies that did not consider the effect of the wake induced by a preceding bubble mainly used the bulk flow velocity or the local velocity estimated by the wall function in the calculation of drag force acting on bubbles. However, this study confirmed that the local liquid velocity could change up to the bubble velocity according to the wake of the bubble.

Based on this observation, it was assumed that the trailing bubble sliding continuously with the preceding bubble has an average value of the bubble velocity and the bulk flow velocity. The maximum distance affected by the preceding bubble was assumed to be twice the bubble diameter and was assumed to decrease linearly as the distance between bubbles increases.

References

- [1] B.U. Bae, Design of condensation heat exchanger for the PAFS (Passive Auxiliary Feedwater System) of APR+ (Advanced Power Reactor Plus), *Annals of Nuclear Energy* 46 (2012) 134–143.
- [2] K.H. Kang, S. Kim, B.U. Bae, Y.J. Cho, Y.S. Park, B.J. Yun, Separate and integral effect tests for validation of cooling and operational performance of the APR+ Passive Auxiliary Feedwater System, *Nuclear Engineering and Technology* 44 (2012) 597–610.
- [3] T.G. Theofanous, C. Liu, S. Additon, S. Angelini, O. Kymäläinen, T. Salmassia, In-vessel coolability and retention of a core melt, *Nuclear Engineering and Design* 169 (1997) 1–48.
- [4] D.H. Lee, I.K. Park, H.Y. Yoon, K.S. Ha, J.J. Jeong, Numerical evaluation of the cooling performance of a core catcher test facility, *Journal of Energy Engineering* 22 (1) (2013) 8–16.
- [5] D. M. Glantz, F.E. Cooke, US Patent No. 5,059,385, 1991.
- [6] G. Sateesh, S.K. Das, A.R. Balakrishnan, Analysis of pool boiling heat transfer: effect of bubbles sliding on the heated surface, *International Journal of Heat and Mass Transfer* 48 (2005) 1543–1553.
- [7] N. Basu, G.R. Warrier, V.K. Dhir, Wall heat flux partitioning during subcooled flow boiling: part 1—model development, *Journal of Heat Transfer* 127 (2005) 131–140.
- [8] G.H. Yeoh, S.C.P. Cheung, J.Y. Tu, M.K.M. Ho, Fundamental consideration of wall heat partition of vertical subcooled boiling flows, *International Journal of Heat and Mass Transfer* 51 (2008) 3840–3853.
- [9] L. Gilman, E. Baglietto, A self-consistent, physics-based boiling heat transfer modeling framework for use in computational fluid dynamics, *International Journal of Multiphase Flow* 95 (2017) 35–53.
- [10] J.C. Chen, Correlation for boiling heat transfer to saturated fluids in convective flow, *Industrial and Engineering Chemistry Process Design and Development* 5 (3) (1966) 322–329.
- [11] S.S. Kutateladze, Boiling heat transfer, *International Journal of Heat and Mass Transfer* 4 (1961) 31–45.
- [12] G.T. Polley, T. Ralston, I.D.R. Grant, Forced crossflow boiling in an ideal in-line tube bundle, in: *Proceedings of the 19th National Heat Transfer Conference*, ASME, New York, NY, 1980 Paper no. USA80-HT-46.
- [13] R.L. Singh, J.S. Saini, H.K. Varma, Effect of cross-flow on boiling heat transfer of refrigerant-12, *International Journal of Heat and Mass Transfer* 28 (2) (1985) 512–514.
- [14] T.H. Hwang, S.C. Yao, Forced convective boiling in horizontal tube bundles, *International Journal of Heat and Mass Transfer* 29 (5) (1986) 785–795.
- [15] R.L. Webb, N.S. Gupte, A critical review of correlations for convective vaporization in tubes and tube banks, *Heat Transfer Engineering* 13 (3) (1992) 58–81.
- [16] N. Kurul, M.Z. Podowski, Multidimensional effects in forced convection sub-cooled boiling, *Heat Transfer Conference* 2 (1990) 21–26.
- [17] J.F. Klausner, R. Mei, D.M. Bernhard, L.Z. Zeng, Vapor bubble departure in forced convection boiling, *International Journal of Heat and Mass Transfer* 36 (3) (1993) 651–662.
- [18] G.H. Yeoh, J.Y. Tu, Population balance modelling for bubbly flows with heat and mass transfer, *Chemical Engineering Science* 59 (15) (2004) 3125–3139.
- [19] B.J. Yun, A. Sławiński, S. Lo, C.H. Song, Prediction of a subcooled boiling flow with advanced two-phase flow models, *Nuclear Engineering and Design* 253 (2012) 351–359.
- [20] R. Sugrue, J. Buongiorno, T. McKrell, An experimental study of bubble departure diameter in subcooled flow boiling including the effects of orientation angle, subcooling, mass flux, heat flux, and pressure, *Nuclear Engineering and Design* 279 (2014) 182–188.
- [21] M. Plesset, S.A. Zwick, The growth of vapor bubbles in superheated liquids, *Journal of Applied Physics* 25 (1954) 493–500.
- [22] L. Scriven, On the dynamics of phase growth, *Chemical Engineering Science* 10 (1959) 1–13.
- [23] N. Zuber, The dynamics of vapor bubbles in nonuniform temperature fields, *International Journal of Heat and Mass Transfer* 2 (1961) 83–98.
- [24] B.B. Mikic, W.M. Rohsenow, P. Griffith, On bubble growth rates, *International Journal of Heat and Mass Transfer* 13 (1970) 657–666.

- [25] H. Ünal, Maximum bubble diameter, maximum bubble-growth time and bubble growth rate during the subcooled nucleate flow boiling of water up to 17.7 MN/m², *International Journal of Heat and Mass Transfer* 19 (1976) 643–649.
- [26] M. Colombo, M. Fairweather, Prediction of bubble departure in forced convection boiling: a mechanistic model, *International Journal of Heat and Mass Transfer* 85 (2015) 135–146.
- [27] N.H. Hoang, I.-C. Chu, D.-J. Euh, C.-H. Song, A mechanistic model for predicting the maximum diameter of vapor bubbles in a subcooled boiling flow, *International Journal of Heat and Mass Transfer* 94 (2016) 174–179.
- [28] S. Maity, Effect of velocity and gravity on bubble dynamics Thesis, University of California Los Angeles, Los Angeles, CA, 2000.
- [29] D. Qiu, V.K. Dhir, Experimental study of flow pattern and heat transfer associated with a bubble sliding on downward facing inclined surfaces, *Experimental Thermal and Fluid Science* 26 (2002) 605–616.
- [30] G. Fiorenza, V. Manzari, C. Pastore, I. Sgura, M. Torresi, C. Gargiulo, An innovative polyimide microchannels cooling system for the pixel sensor of the upgraded ALICE inner tracker, in: Proceedings of the 5th IEEE International Workshop on Advances in Sensors and Interfaces (IWASI), Piscataway, NJ, IEEE, 2013.
- [31] S.H. Cho, S.H. Kim, J.G. Lee, N.-E. Lee, Micro-scale metallization of high aspect-ratio Cu and Au lines on flexible polyimide substrate by electroplating using SU-8 photoresist mask, *Microelectronic Engineering* 77 (2) (2005) 116–124.
- [32] K. Gotoh, Y. Nakata, M. Tagawa, M. Tagawa, Wettability of ultraviolet excimer-exposed PE, PI and PTFE films determined by the contact angle measurements, *Colloids and Surfaces A: Physicochemical and Engineering Aspects* 224 (1) (2003) 165–173.
- [33] Y.N. Kim, J.S. Kim, G.C. Park, H.K. Cho, Measurement of sliding bubble behavior on a horizontal heated tube using a stereoscopic image processing technique, *International Journal of Multiphase Flow* 94 (2017) 156–172.
- [34] R.H. Perry, D.W. Green, J.O. Maloney (Eds.), *Perry's Chemical Engineers' Handbook*, McGraw-Hill, New York, NY, 1997.
- [35] B.U. Bae, B.J. Yun, H.Y. Yoon, C.H. Song, G.C. Park, Analysis of subcooled boiling flow with one-group interfacial area transport equation and bubble lift-off model, *Nuclear Engineering and Design* 240 (9) (2010) 2281–2294.
- [36] G.E. Thornecroft, J.F. Klausner, Bubble forces and detachment models, *Multiphase Science and Technology* 13 (3&4) (2001), doi:[10.1615/MultSciTechn.v13.i3-4.20](https://doi.org/10.1615/MultSciTechn.v13.i3-4.20).